Utah State University

DigitalCommons@USU

Space Dynamics Lab Publications

Space Dynamics Lab

Advanced Mesospheric Temperature Mapper for High-Latitude Airglow Studies

Pierre-Dominique Pautet
Utah State University

Michael J. Taylor
Utah State University

W. R. Pendleton Jr.

Yucheng Zhao
Utah State University

Tao Yuan
Utah State University

R. Esplin

See next page for additional authors

Follow this and additional works at: https://digitalcommons.usu.edu/sdl_pubs

Recommended Citation

Pautet P.-D., Taylor M.J., Pendleton Jr W.R., Zhao Y., Yuan T., Esplin R., and McLain D., An Advanced Mesospheric Temperature Mapper for high-latitude airglow studies, App. Optics, 53 (26), 5934-5943, 2014

UtahState University
MERRILL-CAZIER LIBRARY

Authors

Pierre-Dominique Pautet, Michael J. Taylor, W. R. Pendleton Jr., Yucheng Zhao, Tao Yuan, R. Esplin, and D. McLain

Advanced mesospheric temperature mapper for high-latitude airglow studies

P.-D. Pautet,[1,*] M. J. Taylor,[1] W. R. Pendleton, Jr.,[1] Y. Zhao,[1]
T. Yuan,[1] R. Esplin,[2] and D. McLain[2]

[1]Center for Atmospheric and Space Sciences, Utah State University, Logan, Utah 84322, USA

[2]Space Dynamics Laboratory, Utah State University Research Foundation, Logan, Utah 84341, USA

*Corresponding author: dominiquepautet@gmail.com

Over the past 60 years, ground-based remote sensing measurements of the Earth's mesospheric temperature have been performed using the nighttime hydroxyl (OH) emission, which originates at an altitude of ∼87 km. Several types of instruments have been employed to date: spectrometers, Fabry–Perot or Michelson interferometers, scanning-radiometers, and more recently temperature mappers. Most of them measure the mesospheric temperature in a few sample directions and/or with a limited temporal resolution, restricting their research capabilities to the investigation of larger-scale perturbations such as inertial waves, tides, or planetary waves. The Advanced Mesospheric Temperature Mapper (AMTM) is a novel infrared digital imaging system that measures selected emission lines in the mesospheric OH (3,1) band (at ∼1.5 μm) to create intensity and temperature maps of the mesosphere around 87 km. The data are obtained with an unprecedented spatial (∼0.5 km) and temporal (typically 30″) resolution over a large 120° field of view, allowing detailed measurements of wave propagation and dissipation at the ∼87 km level, even in the presence of strong aurora or under full moon conditions. This paper describes the AMTM characteristics, compares measured temperatures with values obtained by a collocated Na lidar instrument, and presents several examples of temperature maps and nightly keogram representations to illustrate the excellent capabilities of this new instrument.   © 2014 Optical Society of America

OCIS codes: (010.0280) Remote sensing and sensors; (010.1290) Atmospheric optics; (040.3060) Infrared.

http://dx.doi.org/10.1364/AO.53.005934

1. Introduction

Temperature is one of the most essential parameters characterizing the Earth's atmosphere. Knowing its estimate is necessary to define and understand most of the atmospheric processes and to properly quantify their parameterization, especially at mesospheric altitudes and above. The mesosphere lower thermosphere (MLT) region, extending from ∼60 to ∼110 km, is not only the coolest region of the Earth's atmosphere, but also the place where many complex wave processes occur. Unfortunately, it is hardly accessible;

only sounding rocket launches allow direct *in situ* measurements but with very limited temporal and spatial coverage (e.g., see [1]). Continuous satellite measurements can provide a global view of the atmospheric parameters but with a limited resolution (e.g., see [2]). Therefore, ground-based remote-sensing instruments are essential for studying local, short-lived perturbations and define their characteristics.

Several dynamical phenomena associated with planetary waves, tides, gravity waves (GWs), and other short-lived waves affect the Earth's atmosphere. Planetary waves are global-scale perturbations with periods of several days associated with large-scale convective regions or pressure systems [3,4]. Atmospheric tides are the dominant feature of the MLT

region [5]. Their periods are correlated with the duration of a solar or a lunar day (24, 12 h,…). GWs are shorter-period oscillations created by the lifting force of buoyancy and the restoring force of gravity [6]. They can be generated by several sources: in the troposphere by thunderstorm updrafts, frontal systems or airflow over mountains, or by interaction with the polar jet stream. They might also be secondary waves resulting from the breaking of a primary wave which had reached its critical level in the middle or upper atmosphere [7]. These waves propagate vertically and horizontally and may be observed during several hours, with horizontal wavelengths varying from 10 to more than several hundred kilometers. They have a crucial effect on the MLT as they can impact the atmospheric circulation [8]. Freely propagating GWs actively transport energy and momentum from the troposphere to the middle and upper atmosphere, where they deposit their energy and transfer their momentum to the mean flow when breaking in the lower density air [9]. Finally, short-lived (few tens of minutes) waves often called ripples or billows, are small-scale perturbations associated with localized regions of convective or shear instabilities due to the growth of GW amplitude or the Doppler-shifting effect. They are generated *in situ* at the mesospheric altitudes (e.g., see [10,11]) where they create turbulence and mixing.

All these phenomena are relatively well-characterized, but their effects and interactions with the background atmosphere and larger-scale motions remain largely unknown. To fully quantify them, several instruments operating simultaneously are necessary to estimate the horizontal wind and temperature profiles as a function of altitude, as well as their horizontal parameters (wavelength, phase speed, direction of propagation, and wave amplitude). Resonance lidars can provide vertical temperature profiles and possibly wind profiles. Meteor or MF radars are able to give the wind velocities within the MLT region. The horizontal parameters are normally provided by airglow imagers, but they only measure the brightness of different MLT emissions (OH, Na, O_2, and OI) corresponding to the altitudes of the associated emissive layers (87, 90, 94, and 96 km, respectively). This paper will describe a newly designed imager capable of measuring not only the OH emission intensity but also the temperature perturbations at ∼87 km of altitude, generating 2D temperature maps which will help in measuring important GW parameters such as the temperature perturbation amplitude or the phase difference between temperature and intensity. Consequently, this new instrument enables detailed investigations of a broad range of dynamical processes including GW forcing, interaction, filtering, dissipation, and momentum flux deposition (e.g., see [12]). Section 2 of this paper describes how to process the Advanced Mesospheric Temperature Mapper (AMTM) measurements of OH rotational temperature using the intensity of selected emission lines of the OH (3,1)

band. Section 3 depicts the instrument itself, while Section 4 compares temperature measurements with values obtained simultaneously by a collocated Na lidar. Section 5 highlights the capabilities of this instrument with examples of temperature maps and keograms which can be used to define the temperature perturbations propagating through the OH layer. Finally, the conclusion is given in Section 6.

2. Rotational Temperature Measurements

Since their discovery in 1949 by Meinel [13], the rotation–vibration hydroxyl (OH) bands have been extensively used to study the MLT temperature. This part of the atmosphere is hardly accessible; therefore, remote-sensing ground-based measurements are essential to study its characteristics. The equivalence of the OH rotational temperature and the temperature of the emitting atmosphere, established by Wallace [14], makes it possible to measure the mesopause temperature at the altitude of the OH layer.

The hydroxyl molecule is created according to the following exothermic reaction [15–17]:

$$H + O_3 \rightarrow OH * (\nu' \leq 9) + O_2 + 3.3 \text{ eV}. \qquad (1)$$
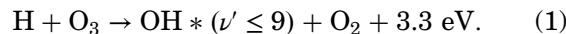
The resulting layer is centered at 86.8 ± 2.6 km and has a thickness of 8.6 ± 3.1 km [18]. The preferred vibration levels are $\nu = 6, 7, 8$, and 9; the molecules in the lower vibration states are created through a radiative cascade from the higher level molecules or by a collisional relaxation mechanism [19].

Several ground-based optical techniques have been used to measure the OH rotational temperature during the past 60 years. More recently, spectrometers (e.g., see [20–23]), near-infrared scanning radiometers [24], and Fabry–Perot or Michelson interferometers [25,26] have provided a wealth of OH temperature measurements. All of these instruments measured the OH rotational temperature, but they are restricted to a small field of view in one (zenith) or a just few look directions. Their temporal resolution is also often limited to several minutes. Several OH rotational bands have been utilized to retrieve the MLT temperature: the most commonly used (6,2) and (8,3) bands are still detectable by CCD-based sensors but are much weaker than the (3,1) or (4,2) bands, which are located further in the infrared part of the spectrum (at ∼1520 and ∼1600 nm, respectively) and require InGaAs or HgCdTe detectors to be measured.

Indium–gallium–arsenide (InGaAs) cameras have a useful spectral range (for a detector cooled to ∼223 K) extending from ∼900 to about 1650 nm. Above this, the photo response decreases rapidly and exhibits a temperature sensitivity which increases as the cutoff wavelength is approached. The brightest OH Meinel bands in this range are the (3,1) and the (4,2) members of the $\Delta v = 2$ sequence, with annual means of 75 ± 18 kR and 106 ± 26 kR, respectively, at mid-latitudes [27]. In view of the

roll-off in detector response through the (4,2) region, the M (3,1) band, with an origin at ~1505 nm, is a better choice to measure the OH M rotational temperature and relative band brightness.

A synthetic spectrum of the OH M night-sky emissions in the spectral interval (1500–1560 nm) is presented in Fig. 1. This region includes the M (3,1) Q-branches near the band origin (~1505 nm) and the first five members of the $P_1(N'')$ and $P_2(N'')$ branches. Additionally, several members of the R_1 and R_2 branches of the (4,2) band are shown (the relatively weak satellite transitions and the non-LTE high-N' transitions are not included). The web-based results were generated using $T_{\text{Rot}} = 190$ K and $T_{\text{Vib}} = 9000$ K, together with the A-coefficients of Mies [28] (see [29] and the web address therein). The prominent $Q_1(1)$ and $P_1(N'')$ ($N'' = 2$, 3, and 4) Λ–doublets are labeled in the figure. These four transitions account for nearly 50% of the total band brightness for a typical rotational temperature of 200 K.

The nominal transmission characteristics of the high-quality, three-cavity bandpass filters used by the AMTM for the (3,1) $P_1(2)$ and $P_1(4)$ measurements are also shown in Fig. 1. This pair of filters is well-matched in peak transmittance, bandpass characteristics, and blocking. In addition, the quantum efficiency of the InGaAs array is nearly the same at the spectral positions of interest, thus yielding a very small instrument correction when inferring the true brightness ratio from the observed value. In operation, the background level is assessed using a four-cavity filter centered near 1521 nm. This region, between the (3,1) $P_2(2)$ and $P_1(2)$ doublets, is quasi-spectral-void under typical nightglow conditions. However, under auroral conditions, the region is contaminated by emissions in the N_2^+ Meinel (1,2) band. Additional information on the filters is provided in Section 3.

The effective rotational temperature T_r is inferred using the line-pair-ratio method introduced by
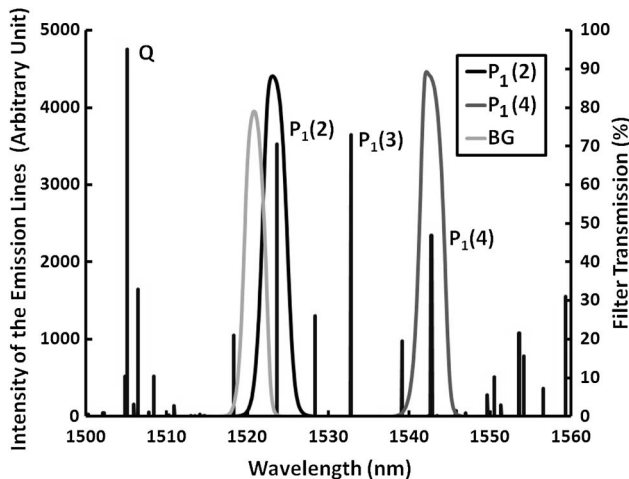

Fig. 1. The (3,1) band of the OH emission spectrum and superposed transmission curves of the narrow-band filters used in the AMTM, as modified from Rousselot *et al.* [29].

Meriwether [30] for the OH M (8,3) band and is concisely presented in more general terms by Makhlouf *et al.* [15]. As indicated above, the brightness ratio of the $P_1(2)$ and $P_1(4)$ Λ–doublets in the (3,1) band is used. The upper levels for these transitions are separated by ~180 cm^{-1} (~0.022 eV) or about 1.3 kT at 200 K. Thus, the exponential factor in the Boltzmann population ratio takes the form

$$\exp[-(E_r/kT_r)] \sim \exp[-(259.58/T_r)]. \qquad (2)$$

Under these conditions, a temperature change of 1% produces changes in the [P1(4)/P1(2)] ratio of 1.75% and 1.10% for temperatures of 150 and 250 K, respectively, encompassing the nominal range for OH M temperatures in the terrestrial mesosphere.

The observed brightness ratio $B_0[P_1(2)]/B_0[P_1(4)]$, after corrections for background differential responsivity and modest contamination of the $P_1(4)$ sample by a weak OH M emission, yields the corresponding ratio of upper-state population when the rovibrational Einstein A-coefficients for transitions are known, i.e.,

$$[N_1(J' = 3.5)/N_1(J' = 1.5)] = \frac{B[P_1(4)]/A[P_1(4)]}{B[P_1(2)]/A[P_1(2)]}, \qquad (3)$$

where the subscripts identify the rovibrational manifold associated with the $\tilde{X}^2\Pi_{3/2}$ fine structure substate and the primes denote upper-state vibration-rotation levels. The expression in Eq. (3) is of general validity, but equating the column population ratio to that of a simple Boltzmann distribution described by a single effective temperature is clearly an approximation.

It is well-established that departures from this model occur for J' values as low as 4.5 in the case of the OH M (7,4) band [31]. However, in the specific case of OH ($X^2\Pi_{3/2}$, $v' = 3$), high-quality FTIR spectroscopic data have validated the model for levels 1.5, 2.5, and 3.5 even under high-latitude (65.2°N) summer conditions [32]. Levels with $J' \geq 4.5$ were not included in the analysis because the associated $P_1(N'')$ transitions were blended with other features or were rather weak. The stringent test of the model was carried out using data wherein the S/N ratio of the $P_1(2)$, $P_1(3)$, and $P_1(4)$ transitions were about 1640, 1570, and 860, respectively.

When the expression in Eq. (3) is equated to the appropriate Boltzmann ratio and the resulting equation solved for T_r, one obtains

$$T_r = \frac{259.58}{\ln(2.644R)}, \qquad (4)$$

where the OH (X, $v' = 3$) term values of Abrams *et al.* [33] and the A-coefficients of Nelson *et al.* [34] have been used. Here, the letter R represents the corrected brightness ratio $B[P_1(2)]/B[P_1(4)]$. It should be noted that correction of the ratio for differential

atmospheric absorption was deemed unnecessary since the FASCOD2-based transmittance calculations of Espy and Hammond [32] yielded $\tau[P_1(4)]/\tau[P_1(2)]$ values of unity within an insignificant 0.3% for the wide range of atmospheric conditions included in their study.

The OH M (3,1) relative band brightness is inferred from the $P_1(2)$ and $P_1(4)$ measurements using the effective rotational temperature from Eq. (4). The decimal fraction of the M (3,1) band brightness reflected in $\{B[P_1(21)] + B[P_1(41)]\}$ varies from ~0.23 when $T_r = 150$ K to ~0.18 at 250 K when the Boltzmann model and the A-coefficients of Nelson *et al.* [34] are used.

3. Instrument Description

At the end of the 1970s, Tepley *et al.* [35] developed a new method using two computerized tilting-filter photometers and a programmable dual-axis mirror to produce maps of the OH (8,3) rotational temperature and intensity to investigate the wave-like structures previously reported in mesospheric observations. Their final images consisted of 121-position arrays (11×11 5 deg pixels). Observations from Arecibo (18.3°N) produced convincing results, but the time of acquisition (~15 min/map) and the poor spatial resolution (10–25 km per "cell") limited the possibility of small-scale GW studies.

In the 1990s, a new CCD-based instrument was developed at Utah State University (USU) to extend the temperature measurements to a larger region of the sky, with better spatial and temporal resolutions. Instead of looking only in one or a few specific directions this instrument images a ~90° area of the sky, centered on the zenith, using a back-illuminated 1024×1024 pixels CCD detector (binned down to 128×128 pixels to improve the signal-to-noise ratio), a telecentric lens system, and 3 narrow-band filters to measure the $P_1(2)$ and $P_1(4)$ lines of the OH (6,2) band and the sky background intensity at 857 nm [36,37]. In 2001, this instrument was improved to include measurements of the intensity of 2 emission lines of the atmospheric O_2 (0,1) band. This emission is located slightly higher (~94 km) than OH, adding complementary altitude information on the atmospheric temperature. The exposure time for each line is typically 60 s, which gives 2 temperature measurements at 2 different altitudes (OH and O_2) every ~5.5 minutes (or one temperature measurement every ~3 minutes in an OH-only mode), but this time, with a separate temperature value for each of the 16,384 pixels of the image.

This USU mesospheric temperature mapper (MTM) has performed extremely well during the past 15 years at: Fort Collins, Colorado (40.5°N), the Starfire Optical Range, New Mexico (35°N), the Bear Lake Observatory, Utah (41.9°N), the Maui Observatory, Hawaii (20.8°N), during 5 years as part of the Maui MALT program, and the Cerro Pachon Observatory, Chile (30.3°S), since 2009. The extensive data sets obtained by the MTM have been used to study long-term temperature variations (e.g., [38]) as well as tidal oscillations [39–41] or more specific GW events [42,43].

Nevertheless, this instrument is limited to mid- and low-latitude observations. At high latitudes, the usual presence of aurora, brighter than the OH emission in the (6,2) band part of the spectrum, contaminates most of the data. Thus, a new MTM has been recently designed specifically for high-latitude and high-resolution research. This time, taking advantage of the recent progress in IR imaging, it was decided to use the OH (3,1) band instead of (6,2). The auroral contamination is much more limited in this part of the spectrum, the (3,1) band is ~70 times brighter than the (6,2) band, and less affected by water vapor absorption. This instrument uses a fast (f:1) 120° field-of-view telecentric lens system designed and built at the Space Dynamics Laboratory (SDL), and three 4″ narrow band (2.5–3 nm) filters centered at 1523 [$P_1(2)$], and 1542 nm [$P_1(4)$] and a nearby background region (BG), mounted in a temperature-controlled filter wheel. The detector is a 320×256 pixels IR sensor, thermoelectrically cooled down to –50°C to limit the electronic noise, and controlled through a USB port by a Windows computer. The telecentric lens system (see Fig. 2) was designed for wide field-of-view narrowband imaging (<2 nm) and has a very high throughput (~1 cm² · sr). Its spectral coverage includes the InGaAs (1100–1600 nm) sensitive range. The exposure time for each filter is short, typically 10 s, giving a temperature measurement every ~30 s (much shorter than the Brunt–Väisälä period) over a ~120° region centered on the zenith. A detailed list of the instrument technical characteristics is given in Table 1.

This AMTM is a significant improvement on the previous instrument. It is ~6 times faster for a ~4
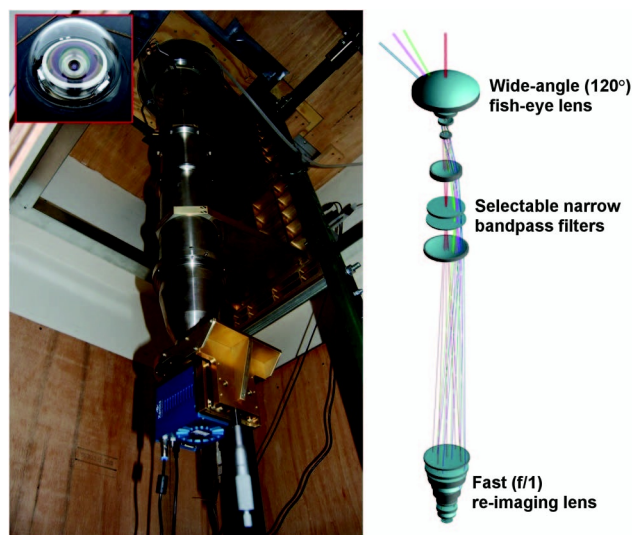

Fig. 2. (Left) AMTM as operated at the Amundsen–Scott South Pole Station (90°S). (Right) Solid sketch design of the AMTM optical system and ray paths for different angles of view.

times better spatial resolution. It can operate in the presence of aurora and also acquires data under full moon condition with very small inconvenience. Two of these instruments have been built so far. The first one operates at the South Pole Station (90°S) since 2010 and the second one at the ALOMAR observatory in Northern Norway (69°N) since the winter of 2010–2011. During the summer months, the latter AMTM is returned to Utah and runs on the USU campus (41.7°N), alongside a Na lidar for cross-calibration and mid-latitude research measurements.

4. Instrument Performance

A. Cross-Calibration

To confirm that the AMTM is accurately measuring the atmospheric temperature at the altitude of the OH layer, it was operated alongside the USU Na lidar during 52 nights in the summers of 2011, 2012, and 2013. This well-proven instrument, which was relocated to USU from its original operational site at Colorado State University (CSU; 41°N, 105°W) in the summer 2010, has operated successfully for more than 20 years. It uses laser-induced fluorescence spectroscopy to study a naturally occurring layer of sodium atoms within the mesopause region, which is formed by the ablation of meteors plunging into the atmosphere. The data are processed to determine the Doppler broadening and frequency shift of the yellow Na emission line, enabling precise measurements of the atmospheric temperature and winds with high vertical and temporal resolutions in the 80–105 km region [44,45].

Figure 3(a) shows the zenith OH (3,1) rotational temperature profile measured by the AMTM during the night of 4–5 September 2012 (UT day 249) and

the Gaussian height-weighted atmospheric temperature centered at 87 km obtained by the USU Na lidar during the same night. The AMTM data were binned to 10-min intervals for direct comparison with the lidar measurements. Each AMTM temperature represents the average value for a 20×20-pixel region centered at the zenith ($\sim 11 \times 11$ km), to encompass the region sampled by the lidar. The lidar data have been processed using a Gaussian function with a FWHM of 9.3 km ($1/e \sim 5.6$ km) height-weighted over the thickness of the emissive layer [39]. Only the lidar values with a measurement error <5 K have been used in this comparison. The weighting was centered at 87 km, which is commonly accepted in the literature as the nominal nocturnal peak altitudes for the OH emission layer [18]. It is clear that the two profiles track each other very well. The average temperatures for the night were 190.7 ± 4.5 K as measured by the AMTM and 190.3 ± 5.4 K according to the lidar data, with the difference being well within the error range of both instruments. Figure 3(b) gives the point-to-point difference between the two data sets. At the beginning of the night, the lidar temperature was a few degrees (<2 K) higher than the AMTM. This trend changed during the course of the night, and after $\sim$6 UT the temperature difference became positive by up to $\sim$2 K. For the whole observation period ($\sim$10 h), $\langle \Delta T \rangle = 0.4 \pm 2.2$ K. This variation can be simply explained by two phenomena: the altitude of the OH layer varied due to geophysical processes like tides or large-scale GWs (e.g., [39]), or the thickness of the layer was modified during the first part of the night. Indeed, after the

Table 1. AMTM Instrument Specifications

| Parameter	Value
Field of view	120°
Throughput/etendue ($A\Omega$)	~ 1 cm$^2 \cdot$ sr
Bandpass filters	
Diameter/Clear aperture	101/94 mm
HPBW ($\Delta\lambda$)	2.3–3.6 nm
Resolving power ($\lambda/\Delta\lambda$)	$700 < - > 450$
Operating temperature	23°C
Temperature coefficient	~ 0.5 Å/°C
Out-of-band transmittance	$<0.001\%$
M(3,1) center wavelengths	
$P_1(2)$	1523.68 nm
$P_1(4)$	1542.79 nm
InGaAs array	
Format/pixel size	$320 \times 256/30$ μm
Quantum efficiency	>0.80
Operating temperature	-50°C
(Ambient ~ 25°C)	
Dark current (HG)	550 counts $\cdot$ s$^{-1} \cdot$ px^{-1}
(all sources at 25°C)	
Read noise (HG/$T_{int} = 100$ μsec)	~ 14 ADU (rms)
System	
Optical transmission	$\sim 50\%$
Responsivity (photon)	~ 0.40 pe $\cdot$ s$^{-1} \cdot$ px^{-1}/R
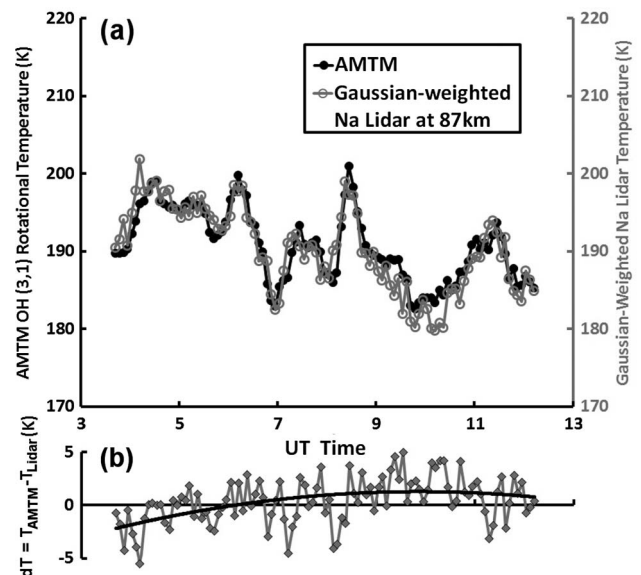
Fig. 3. (a) Zenith temperature time series (black) measured by the AMTM during the night of 4–5 September 2012, from Logan, Utah (41.7°N), compared with the Gaussian height-weighted Na lidar temperature measurements (gray) for the same night. (b) The temperature difference between the two instruments. The slowly increasing trend over the course of the night is most probably due to a semi-diurnal tide modifying the altitude of the OH layer.

evening sunset, removal of the atomic oxygen by three-body recombination creates a decay of the lower part of the hydroxyl layer, changing its barycenter to a slightly higher altitude [46]. Thus, within the comparison capabilities of these 2 instruments, results are identical.

Following the same technique, 50 nights with concurrent observations have been processed to further compare the measurements of the AMTM with the Na lidar temperatures. The observations are summarized in Table 2 and the results are plotted in Fig. 4. Data obtained during the 3 different summer periods (2011, 2012, and 2013) are differentiated to investigate any modification of the AMTM characteristics (sensor quantum efficiency, filters transmission,…) with time, but, as will be shown, none was detected after 3 years. Temperatures were in general higher in 2012 than in 2013 because most of the observations were made in August and September in 2012, while the AMTM operated from end of May to mid-July in 2013, when the mesospheric temperatures are expected to be at their lowest. For these 50 nights, the average temperature difference between the AMTM and the Na lidar was 2.1 ± 3.7 K, which is quite acceptable compared to the instrument errors. Nevertheless, some dissimilarity between the lidar and the AMTM seems to be associated with seasonal change. To investigate that, Fig. 5 shows the temperature difference between the two instruments as a function of the day of the year. An interesting pattern appears: measurements made before day ~200 exhibit an average value of 5.0 K, with a standard deviation of 2.3 K, while the subsequent observations have an average value of −0.3 K, with a standard deviation of 3.2 K. It is well-established that a seasonal change in the mesopause region typically occurs between mid-July and mid-August at ~40°N (8-year climatology from Fort Collins, Colorado 41°N, [47]), with a change in the mesopause altitude from ~86.5 to ~99.5 km. Furthermore, the primary OH M (3,1) emission region is quasi-isothermal in the mean August profile. Hence, it seems likely that the observed change near day 200 is related to this seasonal transition.

Variations during the course of the night may also be due to geophysical processes like tides and/or GWs. Previous observations have shown that the effects of atmospheric tides on the altitude of the OH layer can be significant (i.e., [48–50]), therefore this fact should also be taken into account. Unfortunately, only *in situ* measurements or a triangulation technique using at least two imagers can provide sufficiently accurate information on the location of the
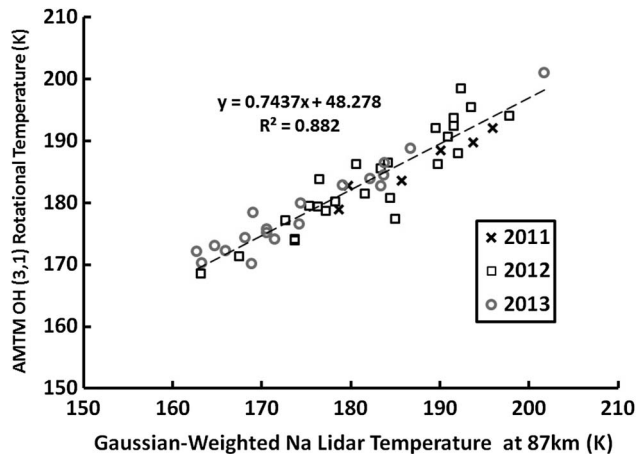

Fig. 4. Comparison of the AMTM temperature nightly averages with the Gaussian height-weighted Na lidar measurements using 50 nights of coincident observations from Logan, Utah (41.7°N), obtained during the summers of 2011, 2012, and 2013.

OH layer, but none was available at the time and place where our observations were made. Nevertheless, the two data sets show very good agreement on individual nights as well as on an average basis, after taking into account the dynamical and chemical processes occurring in the MLT region.

B. Signal-to-Noise Estimate

In order to properly evaluate the signal-to-noise (S/N) ratio for the AMTM instrument, it is necessary to consider a data set with limited atmospheric activity (temperature/intensity perturbations). Figure 6 shows a short-duration sample (60 min, ~120 data points), taken on 20 July 2013, from Logan, Utah, with the raw $P_1(2)$, $P_1(4)$, and BG emission intensities (dots) measured at the zenith over a 1 pixel area (~0.4 × 0.4°). During that time, the atmospheric perturbations were small but to reduce their influence as much as possible, and to better analyze the noise effect, the values obtained by 3-point smoothing processing were removed from the three raw series, then the mean intensities over this 60 min period

Table 2. Total Days (Hours) of Observations

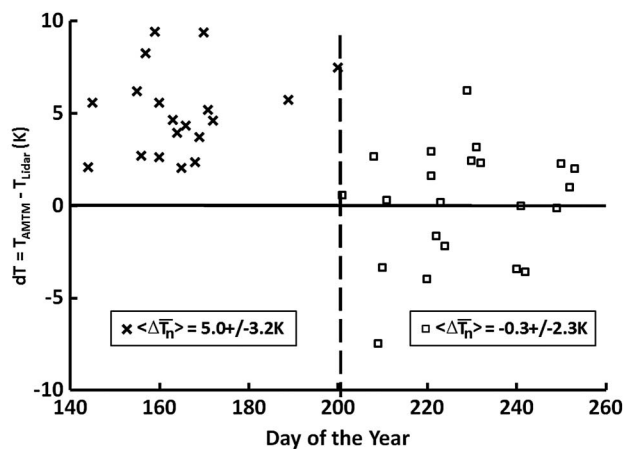|	May	Jun.	Jul.	Aug.	Sep.
2011	0	0	0	4(30)	2(19)
2012	0	5(36)	7(50)	9(77)	4(34)
2013	2(16)	10(72)	4(28)	3(24)	0
Total	2(16)	15(108)	11(78)	16(131)	6(53)

Fig. 5. Distribution of the difference between the AMTM and Na lidar temperatures as a function of the day of the year.
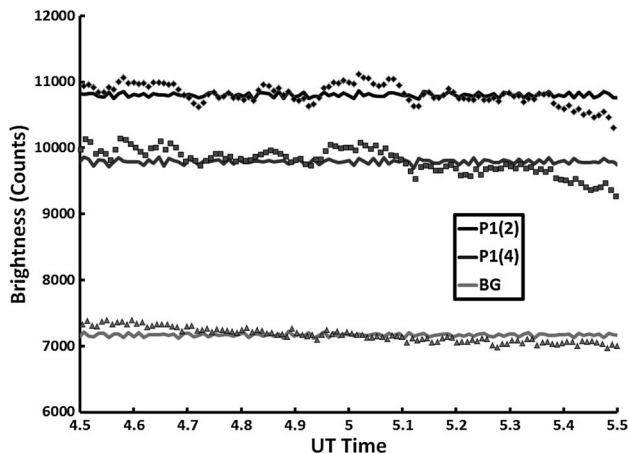
Fig. 6. Sample data set showing the zenith intensity profiles of the three emissions measured by the AMTM [$P_1(2)$, $P_1(4)$, and BG] on 20 July 2013 from Logan, Utah. The dots correspond to the raw intensities while the lines correspond to the filtered values.

were added to the residuals (solid lines). The average intensity values are $10,802 \pm 32$ counts for $P_1(2)$, 9792 ± 35 counts for $P_1(4)$, and $7,178 \pm 24$ counts for BG. The S/N ratios for these emissions are 335.5, 277.4, and 297.9, respectively. The resulting average rotational temperature is 185.0 ± 2.0 K, and finally, the associated signal-to-noise corresponding to this short sample is 92.5.

This value is a good approximation but nevertheless some atmospheric contamination is still present in the zenith profiles, thus the exact AMTM S/N ratio is probably slightly higher. In general, this value also depends on different factors: brightness of the OH emission due to seasonal or geophysical variability, sky conditions at the time of observations (mist, high-altitude clouds), and temperature of the optics (increasing the BG intensity). Our testing of the AMTM S/N shows variations between ~50 to 100 in normal operations mode. For comparison, Table 3 summarizes the S/N ratios for several other instruments which also measure the OH M (3,1) rotational temperature. Though the parameters (FOV, integration time, direction of observation) generally differ between the instruments, an overall comparison shows that the AMTM performance matches or exceeds the previous techniques, and most importantly,

it can provide the mesospheric temperature over a much larger field of view (~200 × 160 km) with high spatial and temporal resolutions.

5. Temperature Maps and Keogram Representations

A. Temperature Maps

One of the main advantages of the AMTM over most of the other instruments in measuring the OH rotational temperature is that it gives a temperature value for each pixel of its sensor, creating a high-resolution "temperature map" over a large region of the upper mesosphere. Thus, it is not only possible to study large-scale dynamical features like tides or planetary waves but also more localized time-varying phenomenon including short-period GWs, bores, instabilities, or wave breaking.

The data are processed to obtain the rotational temperature for each pixel of the image. First, the three series of pictures corresponding to the $P_1(2)$ and the $P_1(4)$ lines and the atmospheric background have to be flat fielded to correct for the nonuniformities of the IR sensor, filters, and optics. Next, for each pixel and for each emission line a time series of intensities is created and fitted to a B-spline curve to determine the interpolated value for a given common instant, since the $P_1(2)$, $P_1(4)$, and BG images are taken at slightly different times. The rotational temperature and relative OH (3,1) band intensity are then processed using these interpolated values, creating two new images: a rotational temperature map and a band intensity map. Finally, these two pictures are spatially calibrated using the known star background and projected onto a 180 × 144 km linear grid to correct for the lens format, assuming a nominal altitude of 87 km for the OH emissive layer [51,52].

Figure 7(a) shows an example temperature map and Fig. 7(b) shows the corresponding relative band intensity image as observed on 1 June 2013 at 6:47 UT from Logan, Utah (41.7°N). Large oscillations due to a short-period GW (observed period ~6.4 min) propagating through the OH layer are clearly visible in both images. The structure on the bottom left is the telescope of the USU Rayleigh lidar, while the curved blue/black sectors at the bottom and on the right are due to the projection process.

Table 3. Performances of Instruments Measuring the OH (3,1) Rotational Temperature

Instrument	FOV	Integration Time	Elevation	Error	S/N
IRFWI Fourier spectrometer Dewan et al. [58]	0.8 × 0.8°	~30 s	Zenith/25°	±0.5–1.5 K	~200
FT spectrometer Mulligan et al. [27]	1.5 × 1.5°	4.5 min	Zenith	as low as ±2 K	<100
Michelson interferometer Azeem and Sivjee [59]	2 × 2°	~5 min	25°	±2 K	~100
GRIPS-6 Bittner et al. [23]	7.9 × 7.9°	15 s	Zenith	±7.5 K	~25
		1 min	Zenith	±2 K	~100
AMTM (This paper)	0.4 × 0.4° (1 pixel)	~30 s	Zenith	±2–4 K	50–100 (typical)

GW parameters were extracted from the Fig. 7 images using well-proven FFT techniques [51,53]. In this case, the horizontal wavelength is 19 ± 3 km, the direction of propagation $305 \pm 5°$ due North, and the observed horizontal phase speed 49 ± 5 m/s. The amplitude perturbation can also be measured using the temperature maps and is equal to 5.1 ± 0.3 K. While the horizontal parameters are typical for short-period GWs propagating through the MLT region, these data provide novel measurements of the temperature perturbations associated with such short-period waves.

B. Keogram Representations

Large-scale GWs or tides are usually not visible in a single temperature map because of their large horizontal wavelengths, which are often greater than the field of view of the imager. To study large-scale atmospheric perturbation, it is necessary to use a different data representation. Keograms, first developed to study auroras, are used to summarize a complete night of observations. They are created by collocating a time series of narrow slices extracted from each image [54]. Two keograms are made for each night: the first one displays the evolution of a North–South
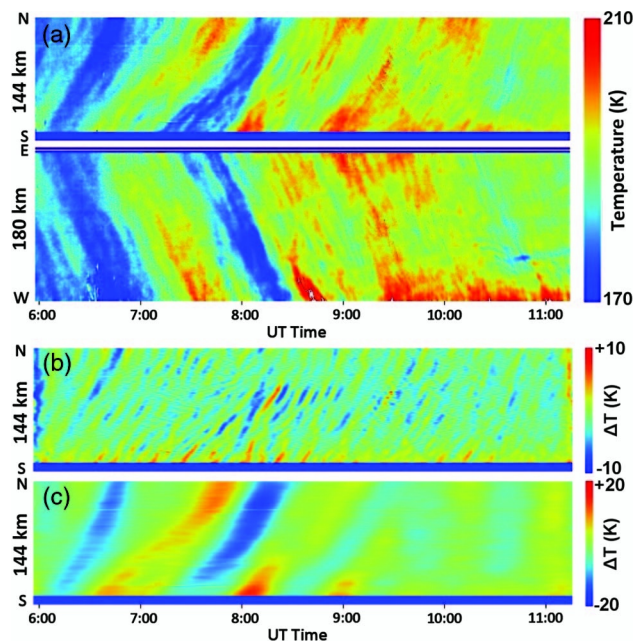
Fig. 8. (a) NS and WE keogram summary of the AMTM temperature measurements obtained during the night of 24 May 2013, from Logan, Utah (41.7°N). Small-scale as well as large-scale perturbations are visible during the whole night. (b) NS keogram filtered using a 5–20 min bandpass Butterworth filter to emphasize the small-period temperature perturbations. (c) NS keogram filtered using a 30–120 min Butterworth filter to emphasize the long-period (~1–1.5 h) temperature perturbations.

band, while the second one shows the evolution of a West–East strip. Figure 8(a) presents the temperature keograms for the night of 24 May 2013, obtained from Logan, Utah (41.7°N). Small-scale GW oscillations with a period around 10 min and temperature amplitude of ~3 K, are visible during the whole night. They can be enhanced by applying a 5–20 min bandpass Butterworth filter on the NS keogram, as shown in Fig. 8(b). Larger perturbations are also evident, especially between 6 and 9 UT where a ~1–1.5 h wave created temperature perturbations with a maximum amplitude of ~10 K, as presented in Fig. 8(c) after application of a 30–120 min filtering process. Furthermore, the temperature varies over the whole observation period (5.5 h); this oscillation is possibly associated with a tidal component.

6. Conclusions

The recently developed Advanced Mesospheric Temperature Mapper (AMTM) is a major step forward for atmospheric research into a "high-resolution" era. Its association with other instruments like lidars or radars operating simultaneously will allow detailed characterization of the atmospheric dynamical features as well as the associated atmospheric background. This new instrument is able to image the temperature perturbations at the 87 km level over a large region of the atmosphere, revealing the effect of the propagation of large-scale as well as short-scale waves on the MLT. Using the OH (3,1) band with a highly sensitive IR detector and a fast optical system
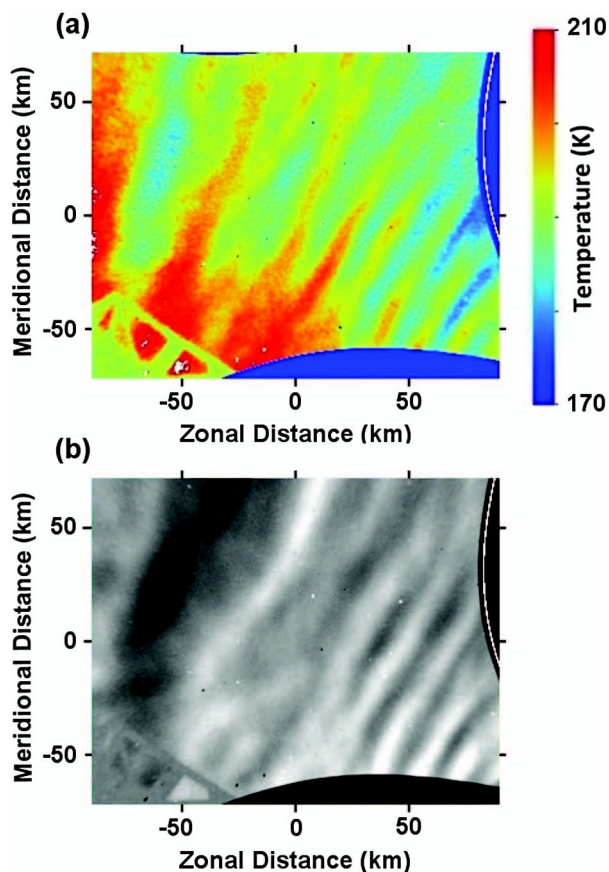

Fig. 7. (Top) OH (3,1) rotational temperature and (bottom) intensity maps taken from Logan, Utah (41.7°N), on 1 June 2013 at 6:47 UT. The perturbations created by a small-scale GW (observed period ~6.4 min) propagating through the OH layer are clearly resolved in both images.

allows high temporal resolution, and thus the detailed investigations of still mostly unknown dynamical processes such as GW-tidal interactions, GW breaking, GW filtering, and momentum flux deposition. Furthermore, the AMTM is a rugged, field-proven instrument and can automatically operate in the presence of aurora or under full moon conditions with minimal inconvenience, allowing nonstop high-latitude observations at remote places such as South Pole or other sites located beyond the Polar Circles, where GW measurements are scarce compared to low- and mid-latitude observations. Its enhanced capability for mapping and quantifying wave-driven dynamics in the upper mesosphere is exceptional. To date, several studies have already utilized the AMTM data to investigate mesospheric temperature inversion layers [55], GW ducting [56], dynamical instability layers [57], or momentum flux associated with GW packets [12], showing promising results.

References

1. R. A. Goldberg, D. C. Fritts, F. J. Schmidlin, B. P. Williams, C. L. Croskey, J. D. Mitchell, M. Friedrich, J. M. Russell III, U. Blum, and K. H. Fricke, "The MaCWAVE program to study gravity wave influences on the polar mesosphere," Ann. Geophys. **24**, 1159–1173 (2006).

2. C. J. Mertens, M. G. Mlynczak, M. Lopez-Puertas, P. P. Wintersteiner, R. H. Picard, J. R. Winick, L. L. Gordley, and J. M. Russell III, "Retrieval of mesospheric and lower thermospheric kinetic temperature from measurements of CO_2 15-mm Earth limb emission under non-LTE conditions," Geophys. Res. Lett. **28**, 1391–1394 (2001).

3. J. R. Holton, *An Introduction to Dynamic Meteorology*, 3rd ed. (Academic, 1992).

4. J. M. Forbes, "Tidal and planetary waves," in *The Upper Mesosphere and Lower Thermosphere: A Review of Experiment and Theory*, R. M. Johnson and T. L. Killeen, eds., Geophysical Monograph Series (AGU, 1995), Vol. **87**, pp. 67–87.

5. S. Chapman and R. S. Lindzen, *Atmospheric Tides* (Springer, 1970).

6. C. O. Hines, "Internal atmospheric gravity waves," Can. J. Phys. **38**, 1441–1481 (1960).

7. S. L. Vadas, D. C. Fritts, and M. J. Alexander, "Mechanism for the generation of secondary waves in wave breaking regions," J. Atmos. Sci. **60**, 194–214 (2003).

8. J. R. Holton, "The influence of gravity wave breaking on the circulation of the middle atmosphere," J. Atmos. Sci. **40**, 2497–2507 (1983).

9. D. C. Fritts and M. J. Alexander, "Gravity wave dynamics and effects in the middle atmosphere," Rev. Geophys. **41**, 1003 (2003).

10. M. J. Taylor and M. A. Hapgood, "On the origin of ripple-type wave structure in the OH nightglow emission," Planet. Space Sci. **38**, 1421–1430 (1990).

11. D. C. Fritts, J. R. Isler, G. E. Thomas, and Ø. Andreassen, "Wave breaking signatures in noctilucent clouds," Geophys. Res. Lett. **20**, 2039–2042 (1993).

12. D. C. Fritts, P.-D. Pautet, K. Bossert, M. J. Taylor, B. P. Williams, H. Iimura, T. Yuan, N. Mitchell, and G. Stöber, "Quantifying gravity wave momentum fluxes with mesospheric temperature mappers and correlative instrumentation," J. Geophys. Res. (submitted).

13. A. B. Meinel, "OH emission bands in the spectrum of the night sky," Astrophys. J. **111**, 555–564 (1950).

14. L. Wallace, "The OH nightglow emission," J. Atmos. Sci. **19**, 1–16 (1962).

15. U. B. Makhlouf, R. H. Picard, and J. R. Winick, "Photochemical-dynamical modeling of the measured response of airglow to gravity waves: 1. Basic model for OH airglow," J. Geophys. Res. **100**, 11289–11311 (1995).

16. S. Adler-Golden, "Kinetic parameters for OH nightglow modeling consistent with recent laboratory measurements," J. Geophys. Res. **102**, 19969–19976 (1997).

17. J. W. Meriwether, Jr., "A review of the photochemistry of selected nightglow emissions from the mesopause," J. Geophys. Res. **94**, 14629–14646 (1989).

18. D. J. Baker and A. T. Stair, Jr., "Rocket measurements of the altitude distribution of the hydroxyl airglow," Phys. Scr. **37**, 611–622 (1988).

19. I. C. McDade, "The altitude dependence of the OH ($X^2\Pi$) vibrational distribution in the nightglow: some model expectations," Planet. Space Sci. **39**, 1049–1057 (1991).

20. G. G. Sivjee and R. M. Hamwey, "Temperature and chemistry of the polar mesopause OH," J. Geophys. Res. **92**, 4663–4672 (1987).

21. G. Hernandez, R. W. Smith, G. J. Fraser, and W. L. Jones, "Large-scale waves in the upper-mesosphere at Antarctic high-latitudes," Geophys. Res. Lett. **19**, 1347–1350 (1992).

22. E. R. Reisin and J. Scheer, "Characteristics of atmospheric waves in the tidal period range derived from zenith observations of O2(0–1) atmospheric and OH(6-2) airglow at lower midlatitudes," J. Geophys. Res. **101**, 21223–21232 (1996).

23. M. Bittner, K. Höppner, C. Pilger, and C. Schmidt, "Mesopause temperature perturbations caused by infrasonic waves as a potential indicator for the detection of tsunamis and other geo-hazards," Nat. Hazards Earth Syst. Sci. **10**, 1431–1442 (2010).

24. R. P. Lowe, "Interferometric spectra of the Earth's airglow (1.2 to 1.6 m)," Phil. Trans. R. Soc. A **264**, 163–170 (1969).

25. S. Sargoytchev, S. Brown, B. H. Solheim, Y.-M. Cho, G. G. Shepherd, and M. J. Lopez-Gonzalez, "Spectral airglow temperature imager (SATI)—a ground based instrument for temperature monitoring of the mesosphere region," Appl. Opt. **43**, 5712–5721 (2004).

26. G. G. Sivjee and R. L. Walterscheid, "Six-hour zonally symmetric tidal oscillations of the winter mesosphere over the South Pole station," Planet. Space Sci. **42**, 447–453 (1994).

27. F. J. Mulligan, D. F. Horgan, J. G. Galligan, and E. M. Griffin, "Mesopause temperatures and integrated band brightnesses calculated from airglow OH emissions recorded at Maynooth (53.2°N 6.4°W) during 1993," J. Atmos. Terr. Phys. **57**, 1623–1637 (1995).

28. F. H. Mies, "Calculated vibrational transition probabilities of OH($X^2\Pi$)," J. Mol. Spectrosc. **53**, 150–188 (1974).

29. P. Rousselot, C. Lidman, J.-G. Cuby, G. Moreels, and G. Monnet, "Night-sky spectral atlas of OH emission lines in the near infrared," Astron. Astrophys. **354**, 1134–1150 (2000).

30. J. W. Meriwether, Jr., "High latitude airglow observations of correlated short-term fluctuations in the hydroxyl Meinel

8–3 band intensity and rotational temperature," Planet. Space Sci. **23**, 1211–1221 (1975).

31. W. R. Pendleton, Jr., P. J. Espy, and M. R. Hammond, "Evidence for non-local thermodynamic equilibrium rotation in the OH nightglow," J. Geophys. Res. **98**, 11567–11579 (1993).
32. P. J. Espy and M. R. Hammond, "Atmospheric transmission coefficients for hydroxyl rotational lines used in rotational temperature determinations," J. Quant. Spectrosc. Radiat. Transfer **54**, 879–889 (1995).
33. M. C. Abrams, D. P. Sumner, M. L. P. Rao, R. Engleman, Jr., and J. W. Brault, "High-resolution Fourier transform spectroscopy of the Meinel system of OH," Astrophys. J. **93**, 351–395 (1994).
34. D. D. Nelson, A. Schiffman, D. J. Nesbitt, J. J. Orlando, and J. B. Burkholder, "H+O3 Fourier-transform H+O3 Fourier-transform infrared emission and laser absorption studies of OH(X²Π) radical: an experimental dipole moment function and state-to-state Einstein A coefficients OH(X²Π) radical: an experimental dipole moment function and state-to-state Einstein A coefficients," J. Chem. Phys. **93**, 7003–7018 (1990).
35. C. A. Tepley, R. G. Burnside, and J. W. Meriwether, Jr., "Horizontal thermal structure of the mesosphere from observations of OH (8-3) band emission," Planet. Space Sci. **29**, 1241–1249 (1981).
36. W. R. Pendleton, Jr., M. J. Taylor, and L. C. Gardner, "Terdiurnal oscillations in OH Meinel rotational temperatures for fall conditions at northern midlatitude sites," Geophys. Res. Lett. **27**, 1799–1802 (2000).
37. M. J. Taylor, L. C. Gardner, and W. R. Pendleton, Jr., "Long period wave signatures in mesospheric OH Meinel (6,2) band intensity and rotational temperature at midlatitudes," Adv. Space Res. **27**, 1171–1179 (2001).
38. Y. Zhao, M. J. Taylor, H.-L. Liu, and R. G. Roble, "Seasonal oscillations in mesospheric temperatures at low-latitudes," J. Atmos. Sol. Terr. Phys. **69**, 2367–2378 (2007).
39. M. J. Taylor, W. R. Pendleton, Jr., C. S. Gardner, and R. J. States, "Comparison of terdiurnal tidal oscillations in mesospheric OH rotational temperature and Na lidar temperature measurements at midlatitudes for fall/spring conditions," Earth Planets Space **51**, 877–885 (1999).
40. Y. Zhao, M. J. Taylor, and X. Chu, "Comparison of simultaneous Na lidar and mesospheric nightglow temperature measurements and the effects of tides on the emission layer heights," J. Geophys. Res. **110**, D09S07 (2005).
41. A. Taori, M. J. Taylor, and S. Franke, "Terdiurnal wave signatures in the upper mesospheric temperature and their association with the wind field at low latitudes (20°N)," J. Geophys. Res. **110**, D09S06 (2005).
42. A. Taori and M. J. Taylor, "Characteristics of wave induced oscillations in the mesospheric O_2 emission intensity and temperature," Geophys. Res. Lett. **33**(2006).
43. D. B. Simkhada, J. B. Snively, M. J. Taylor, and S. J. Franke, "Analysis and modeling of ducted and evanescent gravity waves observed in the Hawaiian airglow," Ann. Geophys. **27**, 3213–3224 (2009).
44. C. Y. She, J. R. Yu, H. Latifi, and R. E. Bills, "High-spectral-resolution fluorescence light detection and ranging for mesospheric sodium temperature measurements," Appl. Opt. **31**, 2095–2106 (1992).
45. T. Yuan, C. Y. She, D. A. Krueger, F. Sassi, R. Garcia, R. G. Roble, H. Liu, H. Schmidt, and S. Reising, "Climatology of mesopause region temperature, zonal wind, and meridional

wind over Fort Collins, Colorado (41°N, 105°W), and comparison with model simulations," J. Geophys. Res. **113**, D03105 (2008).
46. R. P. Lowe, L. M. Leblanc, and K. L. Gilbert, "WINDII/UARS observation of twilight behaviour of the hydroxyl airglow, at mid-latitude equinox," J. Atmos. Terr. Phys. **58**, 1863–1869 (1996).
47. C.-Y. She, S. Chen, Z. Hu, J. Sherman, J. D. Vance, V. Vasoli, M. A. White, J. Yu, and D. A. Krueger, "Eight-year climatology of nocturnal temperature and sodium density in the mesopause region (80 to 105 km) over Fort Collins, CO (41°N, 105°W)," Geophys. Res. Lett. **27**, 3289–3292 (2000).
48. G. G. Shepherd, C. McLandress, and B. H. Solheim, "Tidal influence on O(1 S) airglow altitudes and emission rates at the geographic equator observed by WINDII," Geophys. Res. Lett. **22**, 275–278 (1995).
49. G. R. Swenson and C. S. Gardner, "Analytical models for the responses of the mesospheric OH and Na layers to atmospheric gravity waves," J. Geophys. Res. **103**, 6271–6294 (1998).
50. J. Fujii, T. Nakamura, T. Tsuda, and K. Shiokawa, "Comparison of winds measured by MU radar and Fabry–Perot interferometer and effect of OI5577 airglow height variations," J. Atmos. Sol. Terr. Phys. **66**, 573–583 (2004).
51. F. G. Garcia, M. J. Taylor, and M. C. Kelley, "Two-dimensional spectral analysis of mesospheric airglow image data," Appl. Opt. **36**, 7374–7385 (1997).
52. P.-D. Pautet and G. Moreels, "Ground-based satellite-type images of the upper-atmosphere emissive layer," Appl. Opt. **41**, 823–831 (2002).
53. M. R. Coble, G. C. Papen, and C. S. Gardner, "Computing two-dimensional unambiguous horizontal wavenumber spectra from OH airglow images," IEEE Trans. Geosci. Remote Sens. **36**, 368–382 (1998).
54. M. J. Taylor, P.-D. Pautet, A. F. Medeiros, R. Buriti, J. Fechine, D. C. Fritts, S. L. Vadas, H. Takahashi, and F. T. São Sabbas, "Characteristics of mesospheric gravity waves near the magnetic equator, Brazil, during the SpreadFEx campaign," Ann. Geophys. **26**, 1–12 (2008).
55. T. Yuan, P.-D. Pautet, Y. Zhao, X. Cai, M. J. Taylor, and W. R. Pendleton, Jr., "Coordinated investigation of mid-latitude upper mesospheric temperature inversion layers and the associated gravity wave forcing by Na lidar and Advanced Mesospheric Temperature Mapper in Logan, Utah," J. Geophys. Res. **119**, 3756–3769 (2014).
56. K. Bossert, D. C. Fritts, P.-D. Pautet, M. J. Taylor, B. P. Williams, and W. R. Pendleton, Jr., "Investigation of a mesospheric gravity wave ducting event using coordinated sodium lidar and mesospheric mapper measurements at ALOMAR, Norway (69°N)," J. Geophys. Res., doi:10.1002/2014JD021460 (to be published).
57. X. Cai, T. Yuan, Y. Zhao, P.-D. Pautet, M. J. Taylor, and W. R. Pendleton, Jr., "A coordinated investigation of the creation of two mesospheric dynamical instability layers by a Na Lidar and an Advanced Mesosphere Temperature Mapper over Logan, UT (42°N)," J. Geophys. Res., doi:10.1002/2014JA020131 (to be published).
58. E. M. Dewan, W. R. Pendleton, Jr., N. Grossbard, and P. J. Espy, "Mesospheric OH airglow temperature fluctuations: a spectral analysis," Geophys. Res. Lett. **19**, 597–600 (1992).
59. S. M. I. Azeem and G. G. Sivjee, "Multiyear observations of tidal oscillations in OH M(3,1) rotational temperatures at South Pole, Antarctica," J. Geophys. Res. **114**, A06312 (2009).